EUROPEAN RESPIRATORY *journal*

FLAGSHIP SCIENTIFIC JOURNAL OF ERS

Early View

Original research article

Protease activity sensors enable real-time treatment response monitoring in lymphangioleiomyomatosis

Jesse D. Kirkpatrick, Ava P. Soleimany, Jaideep S. Dudani, Heng-Jia Liu, Hilaire C. Lam, Carmen Priolo, Elizabeth P. Henske, Sangeeta N. Bhatia

Please cite this article as: Kirkpatrick JD, Soleimany AP, Dudani JS, *et al*. Protease activity sensors enable real-time treatment response monitoring in lymphangioleiomyomatosis. *Eur Respir J* 2021; in press (https://doi.org/10.1183/13993003.00664-2021).

This manuscript has recently been accepted for publication in the *European Respiratory Journal*. It is published here in its accepted form prior to copyediting and typesetting by our production team. After these production processes are complete and the authors have approved the resulting proofs, the article will move to the latest issue of the ERJ online.

Copyright ©The authors 2021. For reproduction rights and permissions contact permissions@ersnet.org

Title: Protease activity sensors enable real-time treatment response monitoring in lymphangioleiomyomatosis

Authors: Jesse D. Kirkpatrick[1,2], Ava P. Soleimany[1,2,3], Jaideep S. Dudani[1,4], Heng-Jia Liu[5], Hilaire C. Lam[5], Carmen Priolo[5], Elizabeth P. Henske[5‡], Sangeeta N. Bhatia[1,2,6-10‡]

Affiliations:

[1]Koch Institute for Integrative Cancer Research, Massachusetts Institute of Technology, Cambridge, MA 02139.

[2]Harvard-MIT Division of Health Sciences and Technology, Institute for Medical Engineering and Science, Massachusetts Institute of Technology, Cambridge, MA 02139.

[3]Harvard Graduate Program in Biophysics, Harvard University, Boston, MA 02115.

[4]Department of Biological Engineering, Massachusetts Institute of Technology, Cambridge, MA 02139.

[5]Pulmonary and Critical Care Medicine, Department of Medicine, Brigham and Women's Hospital and Harvard Medical School, Boston, MA.

[6]Howard Hughes Medical Institute, Cambridge, MA 02139.

[7]Department of Electrical Engineering and Computer Science, Massachusetts Institute of Technology, Cambridge, MA 02139.

[8]Department of Medicine, Brigham and Women's Hospital, Harvard Medical School, Boston, MA 02115.

[9]Broad Institute of Massachusetts Institute of Technology and Harvard, Cambridge, MA 02139.

[10]Wyss Institute at Harvard, Boston, MA 02115.

‡These authors co-supervised the study.

Contact information:

Sangeeta N. Bhatia, MD, PhD, 77 Massachusetts Ave. Rm 76-453, Cambridge, MA 02139, Phone: 617-253-0893, Email: sbhatia@mit.edu

Take-home message: Nanoparticles that noninvasively measure the activity of proteases in the lungs enable real-time monitoring of disease progression and therapeutic response in a mouse model of lymphangioleiomyomatosis.

Author contributions:

J.D.K., J.S.D., E.P.H., and S.N.B. initiated the study. J.D.K. and A.P.S. performed experiments and statistical analysis. J.D.K., A.P.S., J.S.D., H-J.L., H.C.L., C.P., E.P.H., and S.N.B. contributed to experimental design and data interpretation. S.N.B. and E.P.H. supervised the research. J.D.K. and S.N.B. wrote the first draft of the manuscript. All authors contributed to writing and editing subsequent drafts of the manuscript and approved the final manuscript.

Funding: This study was supported in part by a Koch Institute Support Grant P30-CA14051 from the National Cancer Institute (Swanson Biotechnology Center), a Core Center Grant P30-ES002109 from the National Institute of Environmental Health Sciences, the Ludwig Fund for Cancer Research, and the Koch Institute Marble Center for Cancer Nanomedicine. J.D.K. acknowledges support from the Ludwig Center fellowship. A.P.S. acknowledges support from the NIH Molecular Biophysics Training Grant (NIH/NIGMS T32 GM008313) and the National Science Foundation Graduate Research Fellowship. J.S.D acknowledges support from the National Science Foundation Graduate Research Fellowship, the Ludwig Center fellowship, and the Siebel Scholar Foundation. S.N.B is a Howard Hughes Medical Institute Investigator.

Abstract

Biomarkers of disease progression and treatment response are urgently needed for patients with lymphangioleiomyomatosis (LAM). Activity-based nanosensors, an emerging biosensor class, detect dysregulated proteases *in vivo* and release a reporter to provide a urinary readout of disease. Because proteases are dysregulated in LAM and may directly contribute to lung function decline, activity-based nanosensors may enable quantitative, real-time monitoring of LAM progression and treatment response. We aimed to assess the diagnostic utility of activity-based nanosensors in a preclinical model of pulmonary LAM.

Tsc2-null cells were injected intravenously into female nude mice to establish a mouse model of pulmonary LAM. A library of 14 activity-based nanosensors, designed to detect proteases across multiple catalytic classes, was administered into the lungs of LAM mice and healthy controls, urine was collected, and mass spectrometry was performed to measure nanosensor cleavage products. Mice were then treated with rapamycin and monitored with activity-based nanosensors. Machine learning was performed to distinguish diseased from healthy and treated from untreated mice.

Multiple activity-based nanosensors [PP03 (cleaved by metallo, aspartic, and cysteine proteases), $P_{adj} < 0.0001$; PP10 (cleaved by serine, aspartic, and cysteine proteases), $P_{adj} = 0.017$)] were differentially cleaved in diseased and healthy lungs, enabling strong classification with a machine learning model ($AUC = 0.95$ from healthy). Within two days after rapamycin initiation, we observed normalization of PP03 and PP10 cleavage, and machine learning enabled accurate classification of treatment response ($AUC = 0.94$ from untreated).

Activity-based nanosensors enable noninvasive, real-time monitoring of disease burden and treatment response in a preclinical model of LAM.

Introduction

Lymphangioleiomyomatosis (LAM) is a rare lung disorder that is characterized by cystic lung destruction, progressive lung function decline, and lung failure [1]. Pathologically, LAM is characterized by abnormal proliferation of smooth muscle-like LAM cells in the lung that may originate from the uterus [2]. LAM cells have bi-allelic loss-of-function mutations in tuberous sclerosis complex (TSC) 1 or 2, which act to inhibit the mechanistic target of rapamycin complex (mTORC1). LAM cells aberrantly express proteases (predominantly matrix metalloproteinases [MMPs] 2 and 9 [3–5] and cathepsin K), which have collagenolytic activity [6] and may contribute directly to lung degradation and cyst formation [7–9]. Consistent with the role of mTORC1 in this disease process, rapamycin is the standard of care for patients with LAM [10, 11]. However, rapamycin treatment is not curative, and the disease progresses when treatment is discontinued, requiring continuous therapy with associated side effects [11, 12]. Currently, pulmonary function tests, including forced expiration volume in 1 second (FEV_1), are the standard method of monitoring disease burden and response to therapy [13]. However, FEV_1 is prone to technical variability [14] and is slow to respond to therapy, hindering clinical decision making and impeding the pace of clinical trials. Therefore, quantitative, accurate, and rapidly responsive biomarkers are urgently needed to monitor patients with LAM and evaluate the efficacy of novel therapies.

Given the limitations of existing biomarkers for LAM, various additional blood biomarkers and imaging tools have been explored [15]. Serum VEGF-D is increased in the majority of patients with LAM [16, 17] and has thus been proposed as a candidate biomarker. However, VEGF-D has suboptimal sensitivity for LAM [17] and its levels do not reliably predict response to therapy [16]. A recent study revealed 32 circulating biomarkers, including VEGF-D, that changed significantly in the serum of LAM patients treated with a combination of rapamycin and hydroxychloroquine

[18]. However, no analyte changes by week 3 of treatment were found to correlate with FEV_1 changes over the 24-week study duration. Finally, high resolution computed tomography has been investigated as a candidate tool for monitoring therapeutic response, but imaging findings have not been shown to change in response to rapamycin treatment [19].

Because dysregulated proteases are a hallmark of LAM, we hypothesized that measuring protease activity could enable accurate and quantitative monitoring of disease. Our group has previously developed "activity-based nanosensors (ABNs)," which measure disease activity *in vivo* by querying protease activity at the site of disease [20–25]. Short, 8-12 amino acid peptide substrates are conjugated to a nanoparticle and administered intravenously or intratracheally. At the disease site, peptide substrates are cleaved by dysregulated proteases, liberating barcoded "reporters" that are cleared into the urine, where they can be detected by mass spectrometry (MS). By appending each substrate with a unique reporter, multiple substrates can be tested simultaneously. Here, we establish the utility of activity-based nanosensors in a novel mouse model of pulmonary LAM. Using machine learning, we build classifiers that accurately read out LAM disease activity and progression and rapidly detect response to rapamycin therapy. Collectively, these results support the clinical development of activity-based nanosensors for monitoring progression and treatment response in LAM.

Methods

Animal experiments

All animal studies were approved by the Massachusetts Institute of Technology (MIT) committee on animal care (protocol 0420-023-23). For all procedures requiring anaesthesia, mice were anesthetized by isoflurane (Zoetis; Parsippany, NJ, USA) inhalation.

Mouse model of pulmonary LAM

105K cells were transduced with a lentivirus encoding for luciferase and a puromycin selection cassette (LP-hLUC-Lv201-0200, Genecopoeia; Rockville, MD, USA), followed by selection with puromycin (1 μg/ml). To establish an *in vivo* LAM model, female nude mice (3-4 weeks old) were injected intravenously with $5x10^5$ luciferized 105K cells (105K-Luc). Disease burden was monitored by IVIS imaging (PerkinElmer; Waltham, MA, USA). For *in vivo* administration, rapamycin was prepared in a vehicle containing 0.25% PEG-200 and 0.25% Tween-80. LAM mice were treated with intraperitoneal injections of rapamycin (LC Labs; Woburn, MA, USA) (1 mg/kg or 3 mg/kg) or vehicle 3-4 times per week and were monitored by IVIS.

***In vivo* disease monitoring with activity-based nanosensors**

Nanosensors (GluFib-Substrate-PEG-8_{40kDa}) for urinary experiments were synthesized by CPC Scientific (San Jose, CA, USA) and sterile filtered with 0.2 μm syringe filters prior to use. Nanosensors were dosed (50 μl total volume, 20 μM concentration per nanosensor) in mannitol buffer (0.28 M mannitol, 5 mM sodium phosphate monobasic, 15 mM sodium phosphate dibasic, pH 7.0-7.5) by intratracheal instillation, immediately followed by a subcutaneous injection of PBS (200 μl) to increase urine production. Bladders were voided 60 minutes after nanosensor administration, and all urine produced 60-120 min after administration was collected. Urine from each mouse was pooled and frozen at -80°C. LC-MS/MS was performed as described previously [21].

Statistical analysis

For all urine experiments, urinary peak area ratio (PAR) values generated by LC-MS/MS were normalized to the PAR of each nanosensor in the injected dose and then mean scaled across all reporters in a given urine sample before further statistical analysis. To identify differential urinary

reporters, all reporters were analysed by unpaired two-tailed *t* test, followed by correction for multiple hypotheses using the Holm-Sidak method in GraphPad Prism 7.0. $P_{adj} < 0.05$ was considered significant. PCA was performed on mean-scaled PAR values and implemented in R using the prcomp package and visualized using ggplot2. For disease classification based on urinary activity-based nanosensor signatures, randomly assigned sets of paired data samples consisting of features (the mean-scaled PAR values) and labels (for example, LAM [18 days] and Rap [+2 days]) were used to train random forest classifiers implemented with the TreeBagger class in MATLAB R2019b. Estimates of out-of-bag error were used for cross-validation, and trained classifiers were tested on randomly assigned, held-out test cohorts. Ten independent train-test trials were run for each classification problem, and classification performance was evaluated with ROC statistics calculated in MATLAB. Classifier performance was reported as the mean accuracy and AUC across the ten independent trials.

Results

Tsc2 deficiency induces protease dysregulation

We first sought to establish a mouse model that captured the dysregulated protease activity that is characteristic of LAM [1]. We leveraged a *Tsc2*-null kidney cystadenoma cell line, termed "105K", that was previously derived from a renal tumour that spontaneously formed in a $Tsc2^{+/-}$ mouse [26]. Analysis of spontaneous mouse kidney cystadenomas similar to those used to isolate the 105K cells revealed punctate expression of MMP2 and MMP9 and intense, ubiquitous expression of CTSK (figure 1a, top). All three proteases were absent in wild type mouse kidneys (figure 1a, bottom). Consistent with reports that LAM-associated CTSK activity is dependent on an acidic microenvironment [27], western blot of lysates from 105K cells cultured at neutral pH

revealed a 37 kDa band corresponding to pro-CTSK [28] (figure 1b). A 27 kDa band, consistent with the size of the active protease form, was detected when recombinantly-expressed mouse CTSK protein was run on the same gel. No anti-CTSK-reactive bands were observed in wild-type mouse kidney or lung homogenates (figure 1b). Finally, we found that 105K cells secreted multiple metalloproteases (MMP2, MMP3, MMP8, and MMP12) *in vitro*, and that expression was significantly abrogated by reintroduction of *Tsc2* (figure 1c).

Tsc2 **null cells are responsive to rapamycin *in vitro* and *in vivo***

The *Tsc1* and *Tsc2* genes encode hamartin and tuberin, respectively, which form a complex to inhibit the mTORC1 cascade [10, 29]. Loss of either hamartin or tuberin results in deregulation of mTOR signalling, and thus uncontrolled cell growth and proliferation. We sought to assess whether rapamycin, an mTOR inhibitor and the first-line therapy in patients with LAM, would inhibit 105K cell growth.

We first treated 105K cells with rapamycin *in vitro* and found that their growth was slowed in a dose-dependent manner (figure S1a). Next, we sought to assess whether 105K cells could be introduced into the lungs of mice to induce disease resembling human LAM. Previous models of LAM have leveraged *Tsc2*-null "TTJ" cells that were passaged as flank tumours to increase aggressiveness, but it was unknown whether the parental "105K" cells would efficiently seed the lungs [9]. To enable *in vivo* tracking of disease burden, we performed lentiviral transduction of 105K cells with a luciferase expression cassette. We then performed tail vein injection of $5x10^5$ luciferase+ 105K (105K-Luc) cells in nude mice and monitored luciferase expression by IVIS. We found that 105K-Luc cells seeded the lungs and formed detectable disease burden within three weeks post inoculation, as assessed by IVIS (figure S1b, top) and histological assessment (figure

S2). These lesions were proliferative, as evidenced by pronounced Ki-67 staining across all lesions (figure S3). To assess the efficacy of rapamycin *in vivo*, we treated mice with rapamycin either immediately after 105K-Luc cell inoculation ("Prevention") or 20 days after inoculation ("Treatment"). We observed very minimal disease in mice treated with rapamycin at day 0 and almost complete regression of disease within 8 days in mice treated at day 20 (figure S1b-c; figure S2).

Tsc2-deficient lesions harbour aberrant protease activity

We next sought to investigate protease activity in *Tsc2*-deficient lesions. We first injected $1x10^6$ 105K cells subcutaneously into the flanks of female nude mice and excised tumours when they reached volumes of ~500 mm^3. We incubated homogenates of these tumours, as well as lungs from healthy nude mice, with a panel of 16 quenched fluorescent protease substrates expected to be broadly cleaved by metallo, serine, and cysteine proteases, and monitored fluorescence over time (figure S4a) [22, 24]. We found that multiple substrates were preferentially cleaved by *Tsc2*-deficient tumor homogenates relative to healthy lung (figure S4b). By subjecting the cleavage data to principal component analysis (PCA), we found that 105K cleavage profiles clustered independently from healthy lungs, demonstrating global differences in proteolytic landscapes (figure S4c). To assess whether these proteolytic differences were preserved when 105K lesions were established in the lungs, we initiated the pulmonary LAM model via intravenous injection of $5x10^5$ 105K-Luc cells and collected bronchoalveolar lavage fluid (BALF) 5, 13, and 19 days later. We incubated BALF from diseased mice at 13 and 19 days, as well as healthy controls, with an additional panel of 16 quenched fluorescent substrates (figure S4d) and found, by PCA, global differences in pulmonary protease activity in diseased and healthy mice that increased with disease

progression (figure S4e). Intriguingly, this study revealed that proteases in both BALF and homogenates from our LAM mouse models preferentially cleaved the substrates PP05 and PQ16, suggesting conservation of protease activity patterns in TSC2-deficient biospecimens regardless of the microenvironment (i.e. flank tumors vs. pulmonary lesions) (figure S4b, d).

We then performed ELISA in BALF to quantify MMP9 and MMP2 concentrations in the lungs of mice with 105K lesions. We observed a striking increase in MMP9 concentration in the BALF of diseased mice 13 (P = 0.0028) and 19 (P = 0.0011) days after 105K cell inoculation (figure S5a). Furthermore, we found that MMP9 concentration correlated with disease burden, as assessed by IVIS (r^2 = 0.63, P = 0.0007) (figure S5b). We observed a trend toward increased MMP2 concentration in BALF of diseased mice at day 19 (P = 0.16) (figure S5c), and found that MMP2 concentration correlated with disease burden (r^2 = 0.49, P = 0.0053) (figure S5d). Immunofluorescence staining revealed ubiquitous cathepsin K expression in 105K lesions at day 19 (figure S6).

Activity-based nanosensors are efficiently cleaved by proteases across catalytic classes

Having established a mouse model of LAM, assessed its responsiveness to rapamycin, and characterized its proteolytic landscape, we next sought to develop activity-based nanosensors tuned to detect these proteases. Because LAM is characterized by broad protease dysregulation, which was recapitulated in our mouse model, we selected a panel of 14 peptide substrates that we had previously found to be cleavable by proteases across multiple classes, including MMPs and cathepsins [21]. We first sought to characterize the sensitivity of each substrate for proteases of different catalytic classes. We synthesized quenched fluorescent versions of each substrate, designed such that fluorescence was activated upon proteolytic cleavage. We incubated each probe

against a recombinant human metalloprotease (MMP2), serine protease (PRSS3), aspartic protease (NAPSA), and cysteine protease (CTSK) at protease concentrations ranging from 10 pM to 10 nM and monitored fluorescence increase over time (figure S7). We found that each probe in the panel had a unique cleavage signature (figure S7, S8) and that each protease was able to cleave at least one probe, with minimum detectable protease concentrations as low as 10 pM after 1 hour of incubation (figure S8, table S1). Thus, we concluded that the 14 nominated peptide substrates provided broad and sensitive coverage of proteases across catalytic classes.

PP03 is cleaved by aspartic proteases in *Tsc2*-deficient lesions under acidic conditions

We next sought to investigate the activity of different classes of proteases in *Tsc2*-deficient tissue and assess the ability of the 14 peptide substrates to detect each protease class. We diluted homogenates of *Tsc2*-deficient 105K cell flank tumors in pH 7.5 buffer and incubated them with each of the 14 fluorogenic peptide substrates, with or without inhibitors of metalloproteases (marimastat), serine proteases [4-(2-aminoethyl)benzenesulfonyl fluoride hydrochloride, AEBSF], cysteine proteases (E64) and aspartic proteases (pepstatin). We found that only marimastat and AEBSF resulted in appreciable abrogation of peptide cleavage, suggesting that only metalloproteases and serine proteases were active in *Tsc2*-deficient tissue under neutral pH conditions (figure S9). Given recent reports of extracellular acidification driving pathological protease activity in LAM [27], we repeated this experiment in acidic (pH 5.25) buffer. Whereas the cleavage of 13 of the 14 peptides significantly decreased at acidic pH, the cleavage of one peptide, PP03, significantly increased (P_{adj} = 0.011) (figure 2a). We therefore hypothesized that PP03 may be cleaved by either aspartic or cysteine proteases, which exhibit optimal activity under acidic conditions, in *Tsc2*-deficient tissue. We found that cleavage of PP03 was almost fully

abrogated by the aspartic protease inhibitor pepstatin at pH 5.25 (P = 0.0017) (figure 2b), but was unaffected by inhibitors against serine, metallo, or cysteine proteases (figure 2c-d). In line with these observations, we found that PP03 was the peptide cleaved most efficiently by the aspartic protease NAPSA in our study (figure 2e). Collectively, these data suggest that the set of 14 substrates broadly detects metallo and serine proteases at neutral pH and PP03 specifically detects aspartic proteases at acidic pH in 105K tumor homogenates.

Activity-based nanosensors enable noninvasive detection of pulmonary 105K lesions in mice

To enable multiplexed protease activity measurement *in vivo*, each of these 14 substrates was uniquely labelled with a mass-encoded urinary reporter. As previously described [20], we used variable labelling of the 14-mer glutamate-fibrinopeptide B (Glu-Fib) with stable isotope-enriched amino acids to uniquely barcode each of the 14 peptide substrates. Multiple reaction monitoring via a liquid chromatography triple quadrupole mass spectrometer (LC-MS/MS) enabled quantitative assessment of urinary reporter concentration within a broad linear range [21]. Finally, these 14 barcoded protease substrates were conjugated to 40 kDa 8-arm poly (ethylene glycol) nanoparticles, as previously described [21].

We then performed intravenous injection of $5x10^5$ 105K-Luc cells and monitored disease development by IVIS (figure S10). We administered the 14-plex nanosensor panel by intratracheal instillation in LAM mice 14 days and 18 days after disease induction (figure 3a). All urine produced between 1 and 2 hours after nanoparticle administration was collected and mass spectrometry was performed. At 14 days, we observed significantly increased pulmonary protease activity against PP03, which we had previously found to be cleaved by aspartic proteases at low pH (figure 2), in LAM mice relative to healthy controls (P_{adj} = 0.034) (figure 3b, left). Furthermore,

among LAM mice at 14 days, PP03 signal was found to positively correlate (r = 0.5871, P = 0.0082) (figure S11a) with disease burden, and two sensors cleaved primarily by serine proteases [21], PP08 (r = -0.6983, P = 0.0009) (figure S11b) and PP11 (r = -0.4617, P = 0.0466) (figure S11c) negatively correlated with disease. Consistent with this finding, at 18 days, cleavage of PP03 was further increased in LAM mice ($P_{adj} = 1.4x10^{-5}$), and cleavage of PP08 (P_{adj} = 0.0047) and PP11 (P_{adj} = 0.026) were significantly decreased (figure 3b, right). On the basis of these differentially cleaved nanosensors, we observed separation of LAM and healthy mice by unsupervised dimensionality reduction with PCA at both tested time points (figure 3c). We then trained a random forest machine learning classifier using a subset of LAM mice and healthy controls from both time points and tested its ability to accurately classify mice in an independent, held-out cohort from the same experiment. We found that the classifier distinguished LAM mice from healthy controls as early as day 14 (AUC = 0.81) and that classification was enhanced at 18 days (AUC = 0.95) (figure 3d). Our results suggest that activity-based nanosensors can measure disease-associated protease dysregulation in a mouse model of pulmonary LAM, enabling accurate disease detection.

Activity-based nanosensors enable rapid treatment response evaluation in LAM mice

We then sought to assess whether activity-based nanosensors could enable objective, quantitative, and rapid assessment of treatment response in LAM. We began treating LAM mice with rapamycin 18 days after disease induction and monitored their pulmonary protease activity with activity-based nanosensors at two and eight days after rapamycin induction. By IVIS, we observed a significant reduction in lung disease burden as early as two days after treatment initiation (P < 0.0001), which further decreased after 8 days (figure S10b). We found that both sensors whose

signal was significantly increased in LAM mice at 18 days, PP03 and PP10, returned to baseline within two days after treatment induction (P_{adj} = N.S. from control) (figure 4a). Notably, we also observed a transient increase above baseline in cleavage of PP04 (P_{adj} = 0.0012 from control) and PP13 (P_{adj} = 0.0042 from control) after rapamycin treatment (figure 4a). Overall, the cleavage of 9 out of 14 nanosensors was significantly altered by treatment with rapamycin, suggesting a profound shift in the pulmonary proteolytic landscape (figure 4b). Consistent with this finding, we found, by PCA, that LAM mice treated with rapamycin for two days clustered separately from both pre-treatment LAM mice and healthy controls (figure 4c, figure S12). However, continued rapamycin treatment for 8 days resulted in pulmonary protease activity that clustered closely with controls. Finally, we trained two random forest classifiers using a subset of LAM mice at day 18 and rapamycin-treated mice after 2 or 8 days of therapy and tested their ability to accurately classify treated and untreated mice in an independent cohort. We found that the classifiers accurately distinguished treated and untreated mice at both tested time points, with the strongest classification at two days after treatment induction (AUC = 0.94) (figure 4d). Therefore, activity-based nanosensors rapidly and reliably detect response to rapamycin in a mouse model of pulmonary LAM.

Discussion

In this work, we demonstrate the utility of activity-based nanosensors for monitoring progression and treatment response in a novel preclinical model of pulmonary LAM. We found that a multiplexed panel of sensors enabled classification of disease, driven primarily by increased pulmonary protease activity against two sensors, PP03 and PP10. Furthermore, we found that this

protease activity returned to baseline two days after treatment initiation, enabling near-perfect classification of treatment response.

Treatment response monitoring via *in vivo* measurements of protease activity offers several advantages over other surrogate endpoints like serum biomarkers, imaging, and spirometry. In LAM, pulmonary protease dysregulation may contribute directly to lung degradation, leading to pulmonary function decline and lung failure [1, 7, 8]. Therefore, measuring protease activity at the site of disease may offer the most direct means of assessing disease activity and predicting long-term outcomes. In contrast, biomarkers found in the blood are inherently correlative, as evidenced by the lack of concordance between changes in serum biomarker concentrations and long-term clinical outcomes in patients with LAM [16]. Though imaging methods like HRCT enable direct visualization of cyst volume, which correlates with pulmonary function, these findings do not appear to reverse in response to treatment [30]. Finally, pulmonary function testing is the gold-standard method for determining pulmonary function, but its utility is limited in treatment response monitoring because of technical variability and long lag times [1]. Although a clinical study would be necessary to fully validate their utility in predicting long-term outcomes, activity-based nanosensors may offer the most direct and rapidly responsive method of reading out disease activity and treatment efficacy in LAM.

Our work also reveals new insights into the biology of disease progression and rapamycin response in our mouse model of LAM. Recent co-culture experiments have shown that extracellular acidification by LAM-associated fibroblasts results in increased expression and activity of the lysosomal protease cathepsin K by *TSC2*$^{-/-}$ cells [27]. Intriguingly, PP03 and PP10, the two nanosensors that were preferentially cleaved in LAM mice, are the only sensors in the panel that are cleaved by the canonical lysosomal proteases NAPSA (figure 2e, figure S7, figure

S8, and table S1) and CTSD [21] under acidic conditions. In this work, we also demonstrated efficient cleavage of PP03 and PP10 by cathepsin K in acidic buffer. Finally, PP03 was the only peptide that was preferentially cleaved by 105K tumor homogenates under acidic conditions. These findings suggest that ABNs may enable real-time monitoring of extracellular acidification and the resulting aberrations in protease activity in LAM. Notably, we found that treatment with rapamycin resulted in a rapid return to healthy levels for both PP03 and PP10, consistent with findings that rapamycin treatment inhibits extracellular acidification and protease activity *in vitro* [27]. The apparent decrease in serine protease activity, as evidenced by the negative correlation between disease burden and urinary PP08 and PP11 signal, may reflect an increase in the expression of serine protease inhibitors over the course of disease progression, a feature of other lung diseases [31, 32], but one that has yet to be described in LAM. Finally, we observed transiently increased cleavage of multiple nanosensors following rapamycin treatment. PP04, the sensor with the most significant increase in cleavage, is most efficiently cleaved *in vitro* by serine proteases, including those involved in the immune response [21]. Although further studies will be necessary to fully elucidate the mechanism underlying this transiently increased protease activity, our results highlight the power of activity-based nanosensors to directly query disease-relevant biological processes *in vivo*.

This work establishes activity-based nanosensors as a new paradigm for monitoring progression and treatment response in LAM, but future studies should address key limitations and unanswered questions. In particular, we did not fully characterize the mouse model described here for evidence of cystic lung destruction, lymphatic involvement, or pulmonary function decline, all of which are hallmarks of LAM in humans [1]. Furthermore, though numerous studies have described dysregulation of metalloproteases [3, 4] and cathepsin K [27] in LAM, a definitive

causative link to disease progression has yet to be established, and a small trial of the MMP inhibitor doxycycline failed to yield clinical benefit in LAM patients [33]. Although we demonstrate that pulmonary cleavage of activity-based nanosensors rapidly responds to treatment with rapamycin in mice, we did not assess whether these changes corresponded to long-term functional outcomes in our mouse model. Clinical trials will be necessary to assess the utility of activity-based nanosensors in predicting long-term response to therapy. Finally, we delivered activity-based nanosensors via intratracheal instillation, but a clinically compatible delivery method such as dry powder inhalation or nebulization will be required for use in humans.

In summary, we have demonstrated the utility of activity-based nanosensors in monitoring progression and treatment response in a mouse model of LAM. Clinically, activity-based nanosensors may enable rapid assessment of treatment response in patients treated with either rapamycin or emerging experimental therapies. By enabling real-time monitoring of disease activity, activity-based nanosensors may dramatically increase the pace of clinical trials and provide accurate and timely information to guide patient care.

Acknowledgments

We thank A. D. Warren for assisting with conceptualization of the study and experimental design, H. E. Fleming for critical editing of the manuscript, A. Mancino (Syneos Health) for performing mass spectrometry, and the Koch Institute Swanson Biotechnology Center, specifically the Histology core and the Preclinical Modeling, Imaging, and Testing core, for technical assistance.

References

1. Henske EP, McCormack FX. Lymphangioleiomyomatosis - A wolf in sheep's clothing. *J. Clin. Invest.* 2012; 122: 3807–3816.
2. Guo M, Yu J, Perl AK, Wikenheiser-Brokamp K, Riccetti M, Zhang E, Sudha P, Adam M, Potter A, Kopras E, Giannikou K, Potter SS, Sherman S, Hammes S, Kwiatkowski D, Whitsett J, McCormack F, Xu Y. Single Cell Transcriptomic Analysis Identifies a Unique Pulmonary Lymphangioleiomyomatosis Cell. *Am. J. Respir. Crit. Care Med.* 2020; : 1–70.
3. Hayashi T, Fleming M V., Stetler-Stevenson WG, Liotta LA, Moss J, Ferrans VJ, Travis WD. Immunohistochemical study of matrix metalloproteinases (MMPs) and their tissue inhibitors (TIMPs) in pulmonary lymphangioleiomyomatosis (LAM). *Hum. Pathol.* 1997; 28: 1071–1078.
4. Matsui K, Takeda K, Yu ZX, Travis WD, Moss J, Ferrans VJ. Role for activation of matrix metalloproteinases in the pathogenesis of pulmonary lymphangioleiomyomatosis. *Arch. Pathol. Lab. Med.* 2000; 124: 267–275.
5. Lee PS, Tsang SW, Moses MA, Trayes-Gibson Z, Hsiao LL, Jensen R, Squillace R, Kwiatkowski DJ. Rapamycin-insensitive up-regulation of MMP2 and other genes in tuberous sclerosis complex 2-deficient lymphangioleiomyomatosis-like cells. *Am. J. Respir. Cell Mol. Biol.* 2010; 42: 227–234.
6. Zhu L, Tang Y, Li X, Keller ET, Yang J, Cho J, Feinberg TY, Weiss SJ. Osteoclast-mediated bone resorption is controlled by a compensatory network of secreted and membrane-tethered metalloproteinases. : 1–16.
7. Babaei-Jadidi R, Dongre A, Miller S, Castellanos Uribe M, Stewart ID, Thompson ZM, Nateri AS, Bradding P, May ST, Clements D, Johnson SR. Mast Cell Tryptase Release

Contributes to Disease Progression in Lymphangioleiomyomatosis. *Am. J. Respir. Crit. Care Med.* 2021; : 1–74.

8. Moses MA, Harper J, Folkman J. Doxycycline treatment for lymphangioleiomyomatosis with urinary monitoring for MMPs [16]. *N. Engl. J. Med.* 2006; 354: 2621–2622.
9. Goncharova E a., Goncharov D a., Fehrenbach M, Khavin I, Ducka B, Hino O, Colby T V., Merrilees MJ, Haczku a., Albelda SM, Krymskaya VP. Prevention of Alveolar Destruction and Airspace Enlargement in a Mouse Model of Pulmonary Lymphangioleiomyomatosis (LAM). *Sci. Transl. Med.* 2012; 4: 154ra134-154ra134.
10. Bissler JJ, McCormack FX, Young LR, Elwing JM, Chuck G, Leonard JM, Schmithorst VJ, Laor T, Brody AS, Bean J, Salisbury S, Franz DN. Sirolimus for Angiomyolipoma in Tuberous Sclerosis Complex or Lymphangioleiomyomatosis. *N. Engl. J. Med.* 2008; 358: 140–151.
11. McCormack FX, Inoue Y, Moss J, Singer LG, Strange C, Nakata K, Barker AF, Chapman JT, Brantly ML, Stocks JM, Brown KK, Lynch 3rd JP, Goldberg HJ, Young LR, Kinder BW, Downey GP, Sullivan EJ, Colby T V, McKay RT, Cohen MM, Korbee L, Taveira-DaSilva AM, Lee HS, Krischer JP, Trapnell BC, National Institutes of Health Rare Lung Diseases C, Group MT. Efficacy and safety of sirolimus in lymphangioleiomyomatosis. *N Engl J Med* 2011; 364: 1595–1606.
12. McCormack FX, Gupta N, Finlay GR, Young LR, Taveira-Da Silva AM, Glasgow CG, Steagall WK, Johnson SR, Sahn SA, Ryu JH, Strange C, Seyama K, Sullivan EJ, Kotloff RM, Downey GP, Chapman JT, Han MK, D'Armiento JM, Inoue Y, Henske EP, Bissler JJ, Colby T V., Kinder BW, Wikenheiser-Brokamp KA, Brown KK, Cordier JF, Meyer C, Cottin V, Brozek JL, Smith K, et al. Official American thoracic society/Japanese

respiratory society clinical practice guidelines: Lymphangioleiomyomatosis diagnosis and management. *Am. J. Respir. Crit. Care Med.* 2016; 194: 748–761.

13. Johnson SR, Cordier JF, Lazor R, Cottin V, Costabel U, Harari S, Reynaud-Gaubert M, Boehler A, Brauner M, Popper H, Bonetti F, Kingswood C, Albera C, Bissler J, Bouros D, Corris P, Donnelly S, Durand C, Egan J, Grutters JC, Hodgson U, Hollis G, Korzeniewska-Kosela M, Kus J, Lacronique J, Lammers JW, McCormack F, Mendes AC, Moss J, Naalsund A, et al. European Respiratory Society guidelines for the diagnosis and management of lymphangioleiomyomatosis. *Eur. Respir. J.* 2010; 35: 14–26.
14. Krowka MJ, Enright PL, Rodarte JR, Hyatt RE. Effect of Effort on Measurement of Forced Expiratory Volume in One Second. *Am. Rev. Respir. Dis.* 1987; 136: 829–833.
15. Nijmeh J, El-Chemaly S, Henske EP. Emerging biomarkers of lymphangioleiomyomatosis. *Expert Rev. Respir. Med.* 2018; 12: 95–102.
16. Young LR, Lee HS, Inoue Y, Moss J, Singer LG, Strange C, Nakata K, Barker AF, Chapman JT, Brantly ML, Stocks JM, Brown KK, Lynch JP, Goldberg HJ, Downey GP, Swigris JJ, Taveira-DaSilva AM, Krischer JP, Trapnell BC, McCormack FX. Serum VEGF-D concentration as a biomarker of lymphangioleiomyomatosis severity and treatment response: A prospective analysis of the Multicenter International Lymphangioleiomyomatosis Efficacy of Sirolimus (MILES) trial. *Lancet Respir. Med.* 2013; 1: 445–452.
17. Young LR, VanDyke R, Gulleman PM, Inoue Y, Brown KK, Schmidt LS, Linehan WM, Hajjar F, Kinder BW, Trapnell BC, Bissler JJ, Franz DN, McCormack FX. Serum vascular endothelial growth factor-D prospectively distinguishes lymphangioleiomyomatosis from other diseases. *Chest* The American College of Chest

Physicians; 2010; 138: 674–681.

18. Lamattina AM, Taveira-Dasilva A, Goldberg HJ, Bagwe S, Cui Y, Rosas IO, Moss J, Henske EP, El-Chemaly S. Circulating Biomarkers From the Phase 1 Trial of Sirolimus and Autophagy Inhibition for Patients With Lymphangioleiomyomatosis. *Chest* Elsevier Inc; 2018; 154: 1070–1082.
19. Yao J, Taveira-DaSilva AM, Jones AM, Julien-Williams P, Stylianou M, Moss J. Sustained effects of sirolimus on lung function and cystic lung lesions in lymphangioleiomyomatosis. *Am. J. Respir. Crit. Care Med.* 2014; 190: 1273–1282.
20. Kwong GA, von Maltzahn G, Murugappan G, Abudayyeh O, Mo S, Papayannopoulos IA, Sverdlov DY, Liu SB, Warren AD, Popov Y, Schuppan D, Bhatia SN. Mass-encoded synthetic biomarkers for multiplexed urinary monitoring of disease. *Nat. Biotechnol.* 2013; 31: 63–70.
21. Kirkpatrick JD, Warren AD, Soleimany AP, Westcott PMK, Voog JC, Martin-Alonso C, Fleming HE, Tammela T, Jacks T, Bhatia SN. Urinary detection of lung cancer in mice via noninvasive pulmonary protease profiling. *Sci. Transl. Med* 2020; 12: 262.
22. Dudani JS, Ibrahim M, Kirkpatrick J, Warren AD, Bhatia SN. Classification of prostate cancer using a protease activity nanosensor library. *Proc. Natl. Acad. Sci.* 2018/08/20. 2018; 115: 201805337.
23. Loynachan CN, Soleimany AP, Dudani JS, Lin Y, Najer A, Bekdemir A, Chen Q, Bhatia SN, Stevens MM. Renal clearable catalytic gold nanoclusters for in vivo disease monitoring. *Nat. Nanotechnol.* Springer US; 2019; 14: 883–890.
24. Soleimany AP, Kirkpatrick JD, Su S, Dudani JS, Zhong Q, Bekdemir A, Bhatia SN. Activatable zymography probes enable in situ localization of protease dysregulation in

cancer. *Cancer Res.* 2021; 81: 213–224.

25. Soleimany AP, Bhatia SN. Activity-Based Diagnostics : An Emerging Paradigm for Disease Detection and Monitoring. *Trends Mol. Med.* Elsevier Ltd; 2020; : 1–19.

26. Parkhitko AA, Priolo C, Coloff JL, Yun J, Wu JJ, Mizumura K, Xu W, Malinowska IA, Yu J, Kwiatkowski DJ, Locasale JW, Asara JM, Choi AMK, Finkel T, Henske EP. Autophagy-dependent metabolic reprogramming sensitizes TSC2-deficient cells to the antimetabolite 6-aminonicotinamide. *Mol. Cancer Res.* 2014; 12: 48–57.

27. Dongre A, Clements D, Fisher AJ, Johnson SR. LAM Cell-Fibroblast Interactions Enhance Protease Activity by Extracellular Acidification. *Am. J. Pathol.* American Society for Investigative Pathology; 2017; 187: 1750–1762.

28. Bossard MJ, Tomaszek TA, Thompson SK, Amegadzie BY, Hanning CR, Jones C, Kurdyla JT, McNulty DE, Drake FH, Gowen M, Levyi MA. Proteolytic activity of human osteoclast cathepsin K: Expression, purification, activation, and substrate identification. *J. Biol. Chem.* 1996; 271: 12517–12524.

29. Crino P, Nathanson K, Henske E. The tuberous sclerosis complex. *N Engl J Med.* 2006; 28;355: 1345–1356.

30. Gopalakrishnan V, Yao J, Steagall WK, Avila NA, Taveira-DaSilva AM, Stylianou M, Chen MY, Moss J. Use of CT Imaging to Quantify Progression and Response to Treatment in Lymphangioleiomyomatosis. *Chest* Elsevier Inc; 2019; 155: 962–971.

31. Vignola AM, Bonanno A, Mirabella A, Riccobono L, Mirabella F, Profita M, Bellia V, Bousquet J, Bonsignore G. Increased levels of elastase and α1-antitrypsin in sputum of asthmatic patients. *Am. J. Respir. Crit. Care Med.* 1998; 157: 505–511.

32. Betsuyaku T, Takeyabu K, Tanino M, Nishimura M. Role of secretory leukocyte protease inhibitor in the development of subclinical emphysema. *Eur. Respir. J.* 2002; 19: 1051–1057.

33. Chang WYC, Cane JL, Kumaran M, Lewis S, Tattersfield AE, Johnson SR. A 2-year randomised placebo-controlled trial of doxycycline for lymphangioleiomyomatosis. *Eur. Respir. J.* 2014; 43: 1114–1123.

Figure Legends

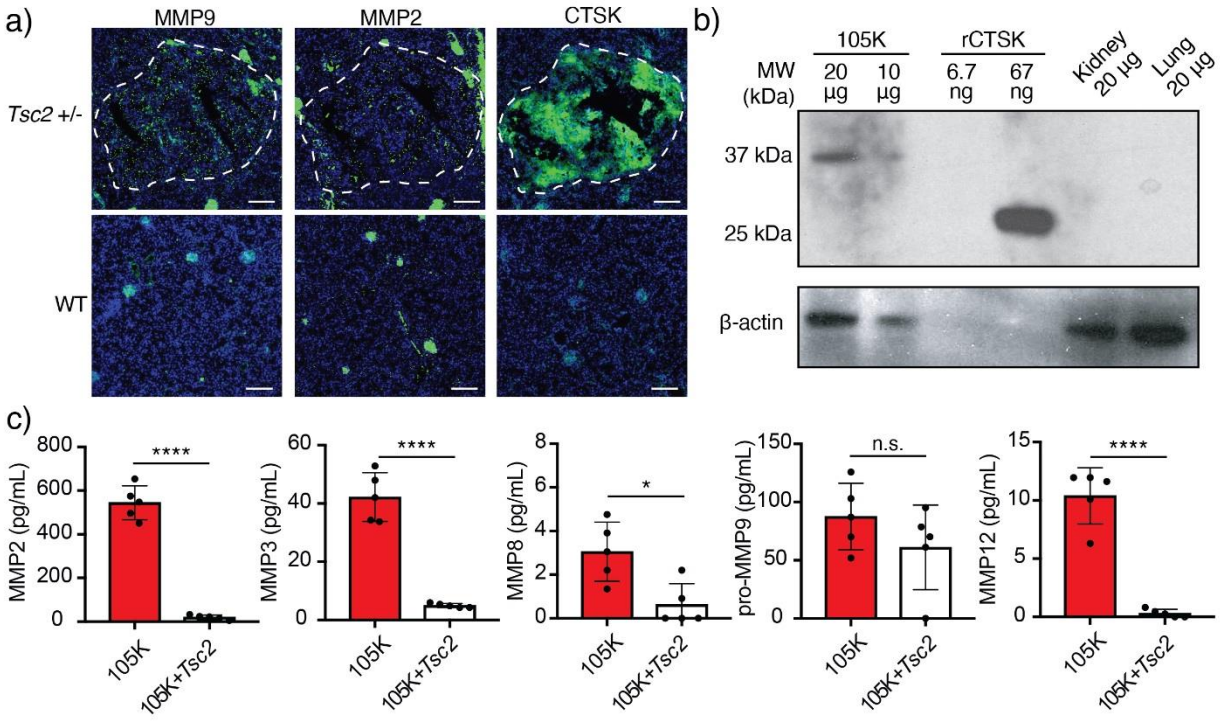

Figure 1: *Tsc2* deficiency results in aberrant protease expression. a) Immunofluorescence staining (green) of MMP9, MMP2, and CTSK in representative primary lesions (outlined in white) that formed spontaneously in the kidneys of *Tsc2*$^{+/-}$ mice (top) compared to kidneys from healthy control mice (bottom). Blue = DAPI (nuclei). Scale = 200 µm. b) Western blot against mouse cathepsin K (CTSK) in 105K cell lysates, recombinant mouse cathepsin K, and healthy mouse kidney and lung. β-actin immunostaining is shown for each sample. Quantity of protein loaded into each lane is noted. c) Expression (mean +/- SD), by multiplexed protein assay, of metalloproteases in conditioned media from 105K cells and 105K cells with retroviral reintroduction of *Tsc2* (n = 5). *P < 0.05, ****P < 0.0001 by two-tailed t test.

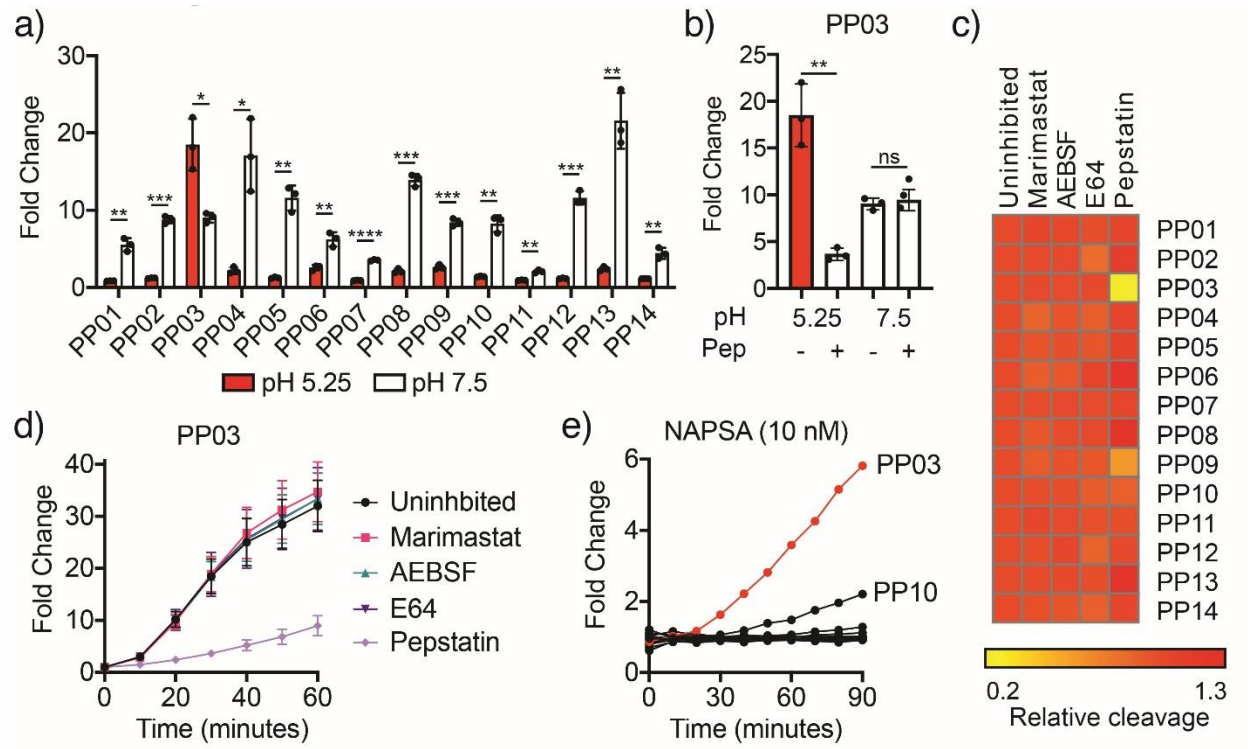

Figure 2: PP03 is cleaved by aspartic proteases in *Tsc2*-deficient lesions at acidic pH. a) Fluorescence fold change of PP01-PP14 after 30 minutes of incubation with 105K tumor homogenates diluted in pH 5.25 (red) or pH 7.5 (white) buffer. *, $P_{adj} < 0.05$; **, $P_{adj} < 0.01$; ***, $P_{adj} < 0.001$; ****, $P_{adj} < 0.0001$ by two-tailed *t* test followed by adjustment for multiple hypotheses with Holm-Sidak correction. b) Fluorescence fold change of PP03 after 30 minutes of incubation with homogenates diluted in pH 5.25 or pH 7.5 buffer, with or without pepstatin ("Pep"). **, $P < 0.01$. c) Substrate cleavage after 30 minutes in homogenates diluted in pH 5.25 buffer incubated with or without inhibitors against metalloproteases (marimastat), serine proteases (AEBSF), cysteine proteases (E64), or aspartic proteases (pepstatin), relative to uninhibited homogenates. d) Fluorescence increase over time of PP03 incubated with homogenates of 105K cell tumors at pH 5.25 with or without protease inhibitors. e) Fluorescence

increase over time of PP01-PP14 incubated with the aspartic protease NAPSA. PP03 is shown in red.

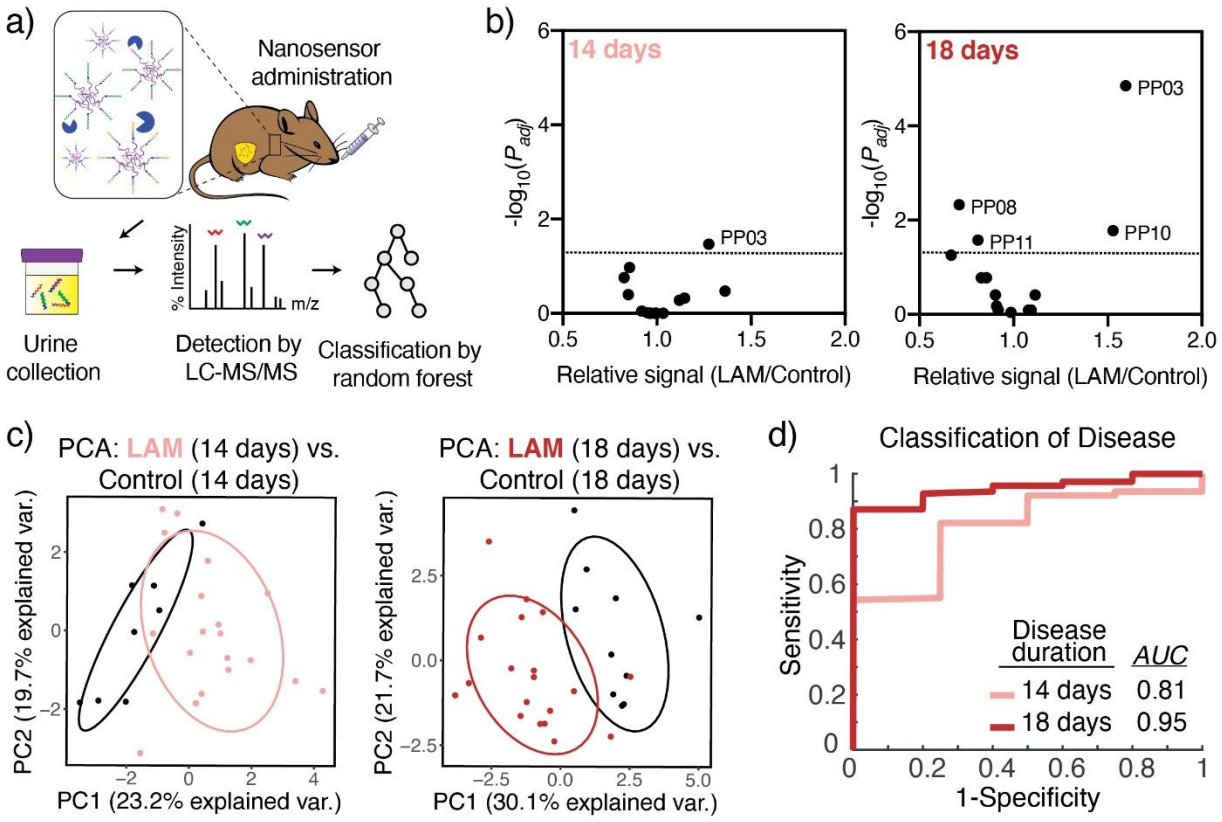

Figure 3: Activity-based nanosensors discriminate LAM mice from healthy controls. a) Schematic of approach. b) Mean scaled urinary reporter concentrations in LAM mice and healthy controls were compared at 14 days (LAM: n = 19; Control: n = 9) and 18 days (LAM: n = 19; Control: n = 10) after disease induction and $-\log_{10}(P_{adj})$ was plotted against fold change between LAM and control. Significance was calculated by two-tailed t test followed by adjustment for multiple hypotheses with Holm-Sidak correction. Dotted line is at P_{adj} = 0.05. c) PCA of urinary reporter output of LAM mice and healthy controls at 14 days and 18 days after disease induction. d) A random forest classifier was trained on urinary reporters from a subset of LAM mice and healthy controls at both 14 (LAM: n = 5; Control: n = 5) and 18 (LAM: n = 5; Control: n = 5) days. ROC curves show performance of this classifier in discriminating LAM mice from healthy controls in an independent test cohort at both 14 (LAM: n = 14; Control: n = 4) and 18 (LAM: n = 14; Control: n = 5) days.

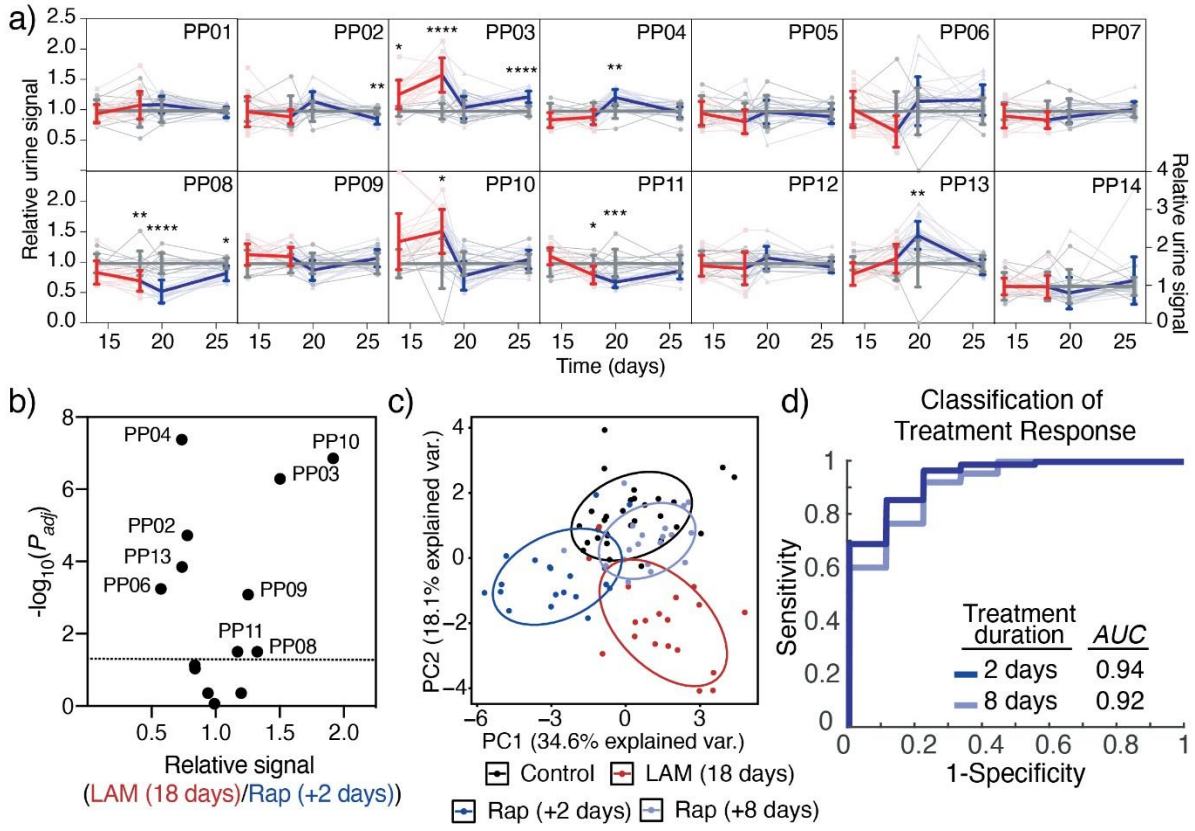

Figure 4: Activity-based nanosensors enable rapid assessment of drug response in LAM. a) Control-normalized urinary reporter signal for each of the 14 ABNs. Transparent lines show ABN trajectories of each mouse over time, while opaque lines are averages over all mice. Red lines represent LAM mice (n = 19) prior to rapamycin treatment and blue lines represent LAM mice treated with 3 mg/kg rapamycin (3-4 times per week). Grey lines represent healthy control mice (n = 10). *P < 0.05, **P < 0.01, ***P < 0.001, ****P < 0.0001 from control. Error bars are SD. For clarity, PP14 is presented on a larger scale y axis. b) Volcano plot showing the significance ($-\log_{10}P_{adj}$) and fold change of each urinary reporter in LAM mice 18 days after 105K-Luc cell injection ("LAM (18 days)") relative to LAM mice after 2 days of rapamycin treatment ("Rap (+2 days)"). Dotted line is at P_{adj} = 0.05. c) Mean scaled urinary reporter concentrations were

normalized to matched controls at each time point and subjected to PCA. d) Two random forest classifiers were trained on urinary reporters from a subset of LAM (18 days) mice (n = 10) and either Rap (+2 days) (n = 10) or Rap (+8 days) (n = 10) mice. ROC curves show performance of these classifiers in discriminating Rap (+2 days) (n = 9) and Rap (+8 days) (n = 9) mice from untreated LAM (18 days) (n = 9) mice in independent, held out test cohorts from the same experiment.

Online Data Supplement

Title: Protease activity sensors enable real-time treatment response monitoring in lymphangioleiomyomatosis

Authors: Jesse D. Kirkpatrick, Ava P. Soleimany, Jaideep S. Dudani, Heng-Jia Liu, Hilaire C. Lam, Carmen Priolo, Elizabeth P. Henske, Sangeeta N. Bhatia

Supplementary Methods

Immunofluorescence staining

Kidneys were excised from 7-month-old *Tsc2*$^{+/-}$ and WT AJ mice and fresh frozen in optimal cutting temperature (OCT) media (Sakura; Torrance, CA, USA). Sections were stained with rabbit IgG isotype control (ThermoFisher, #31235; Waltham, MA, USA) (2 µg/ml in block buffer) and primary antibodies against mouse MMP9 (Abcam, ab137867; Cambridge, MA, USA) (1:250 dilution in block buffer), MMP2 (Abcam, ab37150, 1:200 dilution in block buffer), and CTSK (Abcam, ab19027, 1:250 dilution in block buffer) for 2.5 hours at RT. Lungs were excised from either healthy female nude mice or 19 days after intravenous inoculation with $5x10^5$ 105K cells. Lungs were filled with OCT media, embedded, cryosectioned, and stained for Ki-67 (Abcam, ab15580, 1 ug/mL in block buffer) and cathepsin K (Abcam, ab19027, 1 ug/mL in block buffer) for 1 hour at RT. Slides were imaged using a Pannoramic P250 whole slide scanner (3DHistech; Budapest, Hungary).

Cell lines

Tsc2-null 105K cells were previously derived from a *Tsc2*$^{+/-}$ C57BL/6J mouse renal tumour as described (17). 105K+*Tsc2* cells were generated via retroviral reintroduction of *Tsc2*, as previously described (18, 19). 105K and 105K+*Tsc2* cells were cultured in Dulbecco's modified Eagle medium supplemented with 10% foetal bovine serum and 1% penicillin-streptomycin.

Western blot for CTSK

105K cells were lysed in RIPA buffer supplemented with protease inhibitors. Normal kidney and lung were harvested from healthy mice, snap frozen in liquid nitrogen, and subsequently homogenized in ice cold RIPA buffer with protease inhibitors. Recombinant active mouse cathepsin K (Biovision; Milpitas, CA, USA) was used as a positive control. Samples were loaded

into NuPAGE Bis-Tris Mini Gels (Invitrogen; Carlsbad, CA, USA) and western blot was performed. Membranes were subsequently stained for cathepsin K (ab19027, Abcam, 1:1000 in 5% milk) and β-actin (ab8227, Abcam, 1:1000 in 5% milk).

Rapamycin dose response in 105K cells

Rapamycin (LC Labs) was reconstituted in ethanol. 105K cells were plated at 5,000 cells/well in 24-well plates and treated with either vehicle (0.002% ethanol) or rapamycin at 2 nM, 20 nM, or 200 nM. Cells were trypsinized and counted at each time point.

***Ex vivo* protease substrate screening**

To establish flank tumours, $1x10^6$ 105K cells (P20) were injected subcutaneously in female nude mice (3-4 weeks old) and grown until tumour volumes were approximately 500 mm^3. Mice were euthanized and tumours and healthy lungs were extracted, flash frozen in liquid nitrogen, and homogenized in PBS using MACS M tubes (Miltenyi Biotec; Somerville, MA, USA) according to manufacturer's protocol. Sixteen previously reported protease-cleavable substrates (14) flanked by a fluorophore (5-carboxyfluorescein) and quencher (CPQ2) were synthesized by CPC Scientific. Homogenates were diluted to 200 mg of tissue/ml in PBS and incubated with fluorogenic substrates (0.33 μM final concentration) at 30 μl final volume at 37 ºC for 30 min. For the protease inhibitor ablation study, homogenates were further diluted 5-fold in either pH 7.5 buffer containing 50 mM Tris, 10 mM $CaCl_2$, 300 mM NaCl, 20 μM $ZnCl_2$, 0.02% Brij-35, and 1% bovine serum albumin (BSA) or pH 5.25 buffer containing 50 mM sodium acetate, 2.5 mM EDTA, 1 mM DTT, 0.01% Triton X-100, and 1% BSA and pre-incubated with either marimastat (1 mM), 4-(2-aminoethyl)benzenesulfonyl fluoride hydrochloride (400 μM), E64 (100 μM), or pepstatin (4 μM) for 30 minutes. Fluorogenic substrates were then added at 10 μM final concentration and cleavage was allowed to proceed for 60 min at 37 ºC. For BALF experiments,

the pulmonary LAM model was initiated, as described in the main methods. After 13 and 19 days, mice were euthanized by isoflurane overdose, and BALF was collected as previously described, with a single 1 ml injection of cold PBS (20). Centrifugation at 8,000xg for 5 minutes was performed at 4 ºC to remove debris. BALF was incubated with a panel of 16 fluorogenic substrates (0.33 μM final concentration) at 30 μl final volume at 37 ºC for 45 min. For all *ex vivo* protease activity experiments, proteolytic cleavage of substrates was quantified by increases in fluorescence over time by fluorimeter (Tecan Infinite M200 Pro; Männedorf, Switzerland).

Recombinant protease screening

Recombinant human MMP2 (Enzo), PRSS3 (R&D Systems), NAPSA (R&D Systems) and CTSK (Enzo) were incubated with each fluorogenic peptide substrate (5 μM final concentration) at enzyme concentrations ranging from 10 pM to 10 nM and fluorescence increase over time was measured for 90 min by fluorimeter at 37 ºC. MMP2 buffer consisted of 50 mM Tris, 10 mM $CaCl_2$, 300 mM NaCl, 20 μM $ZnCl_2$, 0.02% Brij-35, and 1% BSA (pH 7.5); PRSS3 buffer consisted of 50 mM Tris, 150 mM NaCl, 10 mM $CaCl_2$, 0.05% Brij-35, and 1% BSA (pH 7.5); NAPSA buffer consisted of 100 mM NaOAc, 200 mM NaCl, and 1% BSA (pH 3.5); CTSK buffer consisted of 50 mM NaOAc, 2.5 mM EDTA, 1 mM DTT, 0.01% Triton X-100, and 1% BSA (pH 5.5).

Multiplexed protein assay

105K and 105K+*Tsc2* cells were plated in 6-well plates (250,000 cells/well) and allowed to adhere for 1 day. Media was replaced with serum-free media and supernatant was collected after 1 day. Metalloprotease concentrations were quantified using a multiplexed protein assay (Eve Technologies; Calgary, Alberta, Canada).

ELISA

For quantification of pulmonary protease concentrations, BALF was collected as described above and concentrations of MMP9 (MMPT90, R&D Systems; Minneapolis, MN, USA) and MMP2 (MMP200, R&D Systems) were measured by ELISA, according to the manufacturer's protocol.

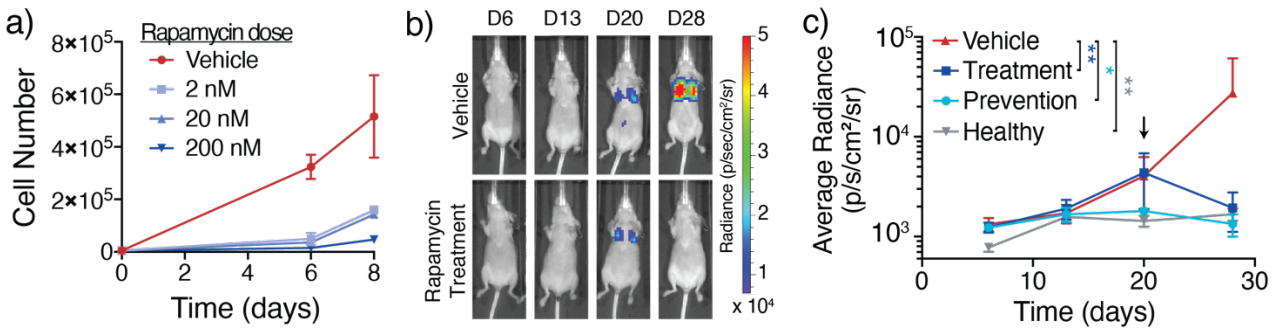

Figure S1: *Tsc2*-deficient 105K cells are responsive to rapamycin *in vitro* and *in vivo*. a) Cell growth over time is shown for 105K cells treated with various doses of rapamycin or vehicle (ethanol) (n = 2 wells each time point). b) Representative IVIS images of 105K-Luc-inoculated mice treated with either vehicle or rapamycin (1 mg/kg) 20 days after intravenous injection of 105K-Luc cells. c) Quantification of lung luminescence in 105K-Luc-injected mice treated with vehicle from day 20 ("Vehicle"), rapamycin from day 20 ("Treatment"), or rapamycin from day 0 ("Prevention"), and healthy controls ("Healthy") (n = 4 to 5 per group). Arrow denotes the time at which rapamycin was initiated in the "Treatment" group. *$P < 0.05$, **$P < 0.01$ from "Vehicle" at day 28 by Mann-Whitney test. Error bars are SD.

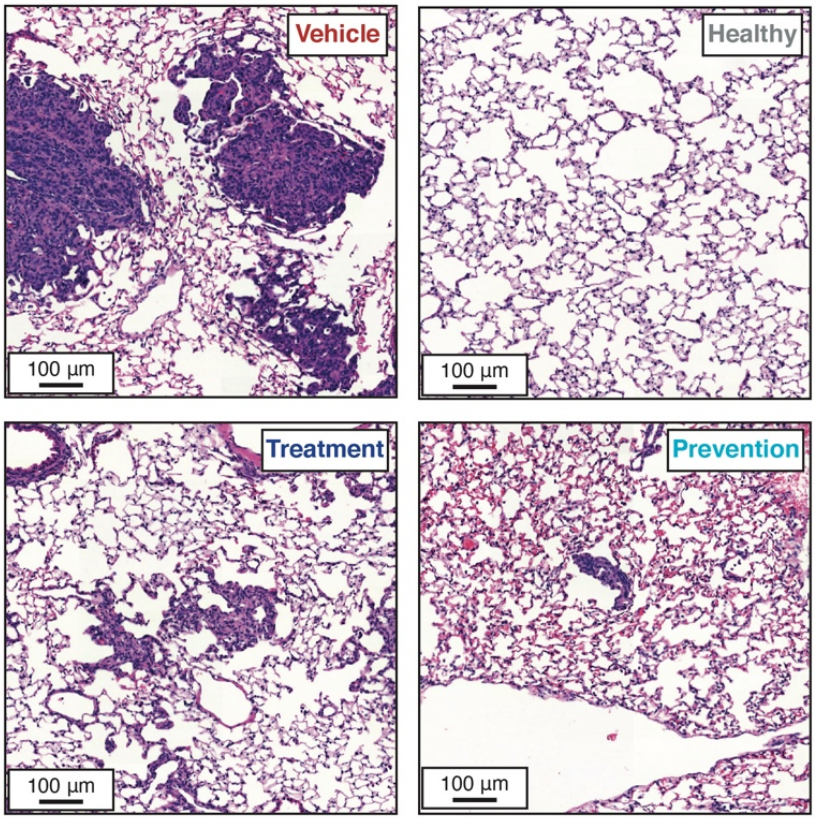

Figure S2: 105K cell lesions respond to rapamycin treatment. Representative H&E images of lungs from 105K-Luc-injected mice ("Vehicle"), healthy control mice ("Healthy"), and 105K-Luc-injected mice treated with rapamycin at either day 20 (3 mg/kg, "Treatment") or day 0 (1 mg/kg, "Prevention").

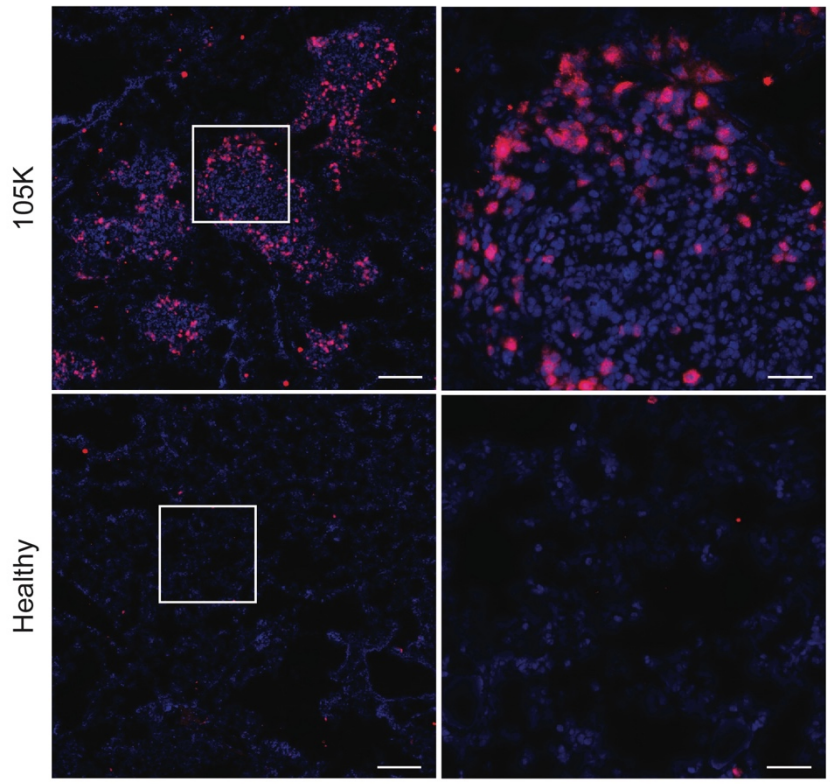

Figure S3: 105K lesions are proliferative. Immunofluorescence images of Ki-67 staining (red) in mouse lungs 19 days after intravenous injection with 105K cells (top) and in healthy control lungs (bottom). Images are shown at low (scale = 200 um, left) and high (scale = 50 um, right) magnification. Nuclei are shown in blue.

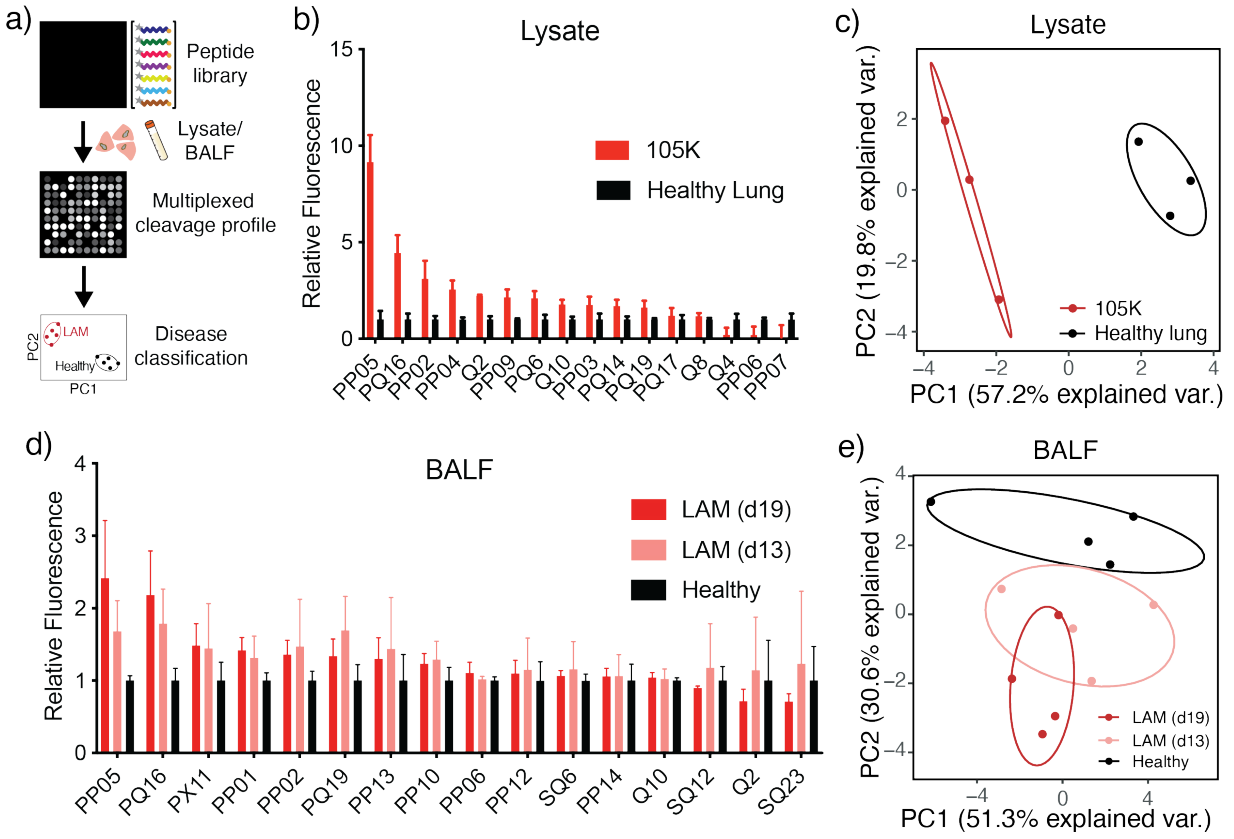

Figure S4: Protease activity is dysregulated in LAM mouse model. a) Tissue lysates and bronchoalveolar lavage fluid (BALF) were incubated with quenched fluorescent protease substrates, enabling quantification of protease activity dysregulation and assessment of global differences by PCA. b) Cleavage of peptides incubated with homogenates of 105K cell flank tumors for 30 minutes, relative to cleavage by homogenates of healthy lung. c) PCA of lysate cleavage data at 30 minutes. d) Cleavage of peptides incubated with BALF from LAM mice at day 13 (d13) or day 19 (d19) for 45 minutes, relative to cleavage by BALF from healthy mice. e) PCA of BALF cleavage data at 45 minutes.

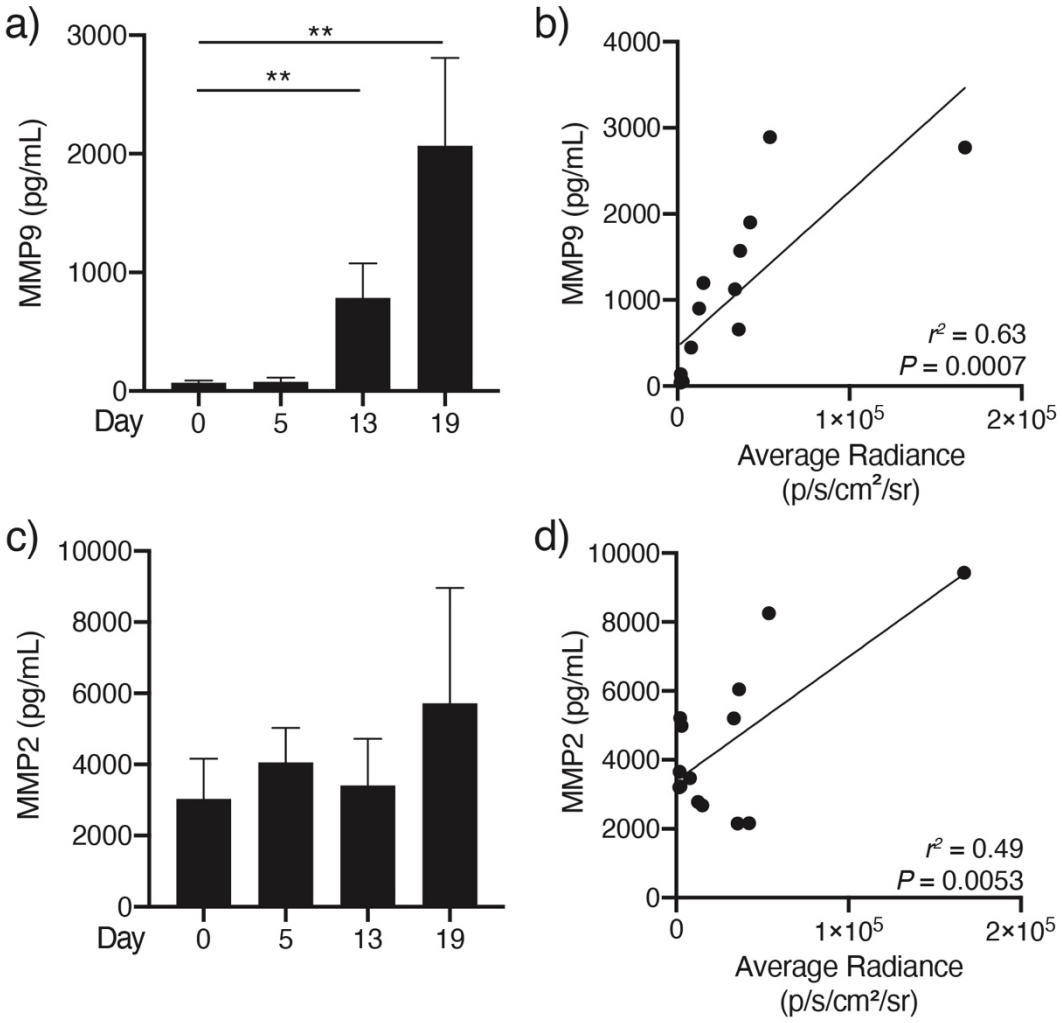

Figure S5: MMPs are dysregulated in mouse model of pulmonary LAM. a) Concentration of MMP9 (pg/ml) in BALF from mice intravenously inoculated with 105K cells. $^{**}P < 0.01$ by unpaired two-tailed *t* test. b) Linear regression of MMP9 concentration (y-axis) with disease burden as assessed by IVIS (x-axis). c) Concentration of MMP2 (pg/ml) in BALF from mice intravenously inoculated with 105K cells. d) Linear regression of MMP2 concentration (y-axis) with disease burden as assessed by IVIS (x-axis). n = 4-5 mice per time point.

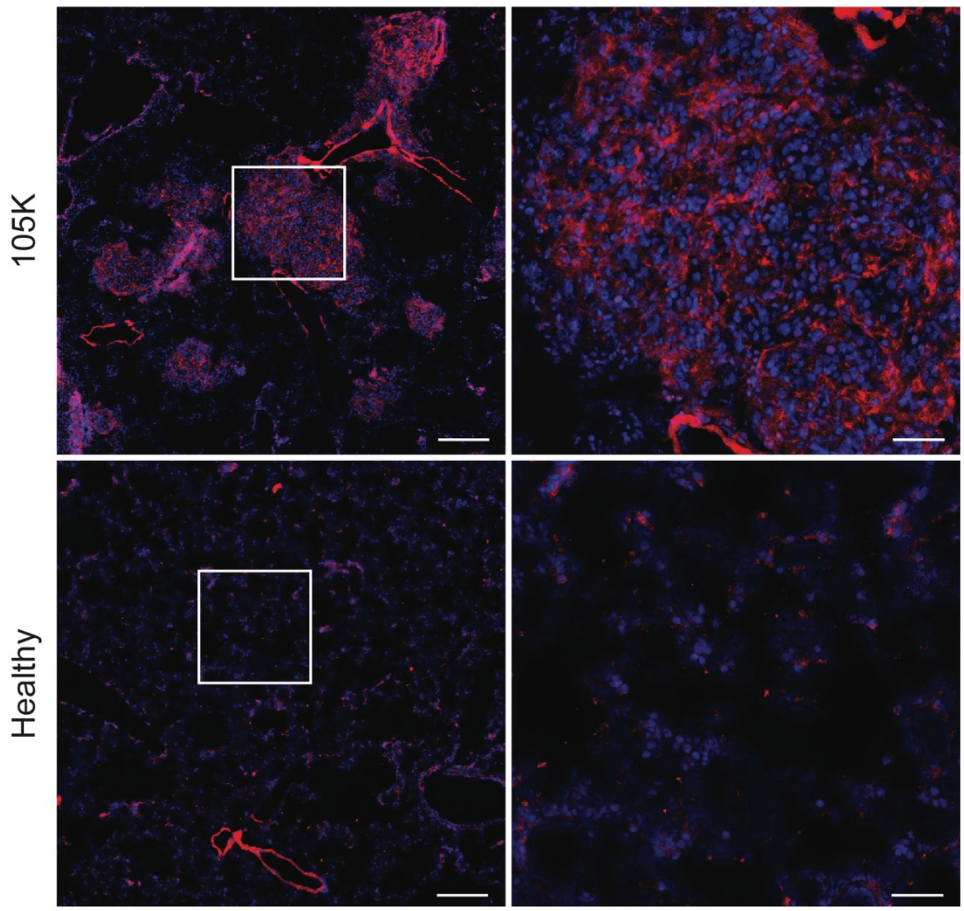

Figure S6: 105K lesions express cathepsin K. Immunofluorescence images of cathepsin K staining (red) in mouse lungs 19 days after intravenous injection with 105K cells (top) and in healthy control lungs (bottom). Images are shown at low (scale = 200 um, left) and high (scale = 50 um, right) magnification. Nuclei are shown in blue.

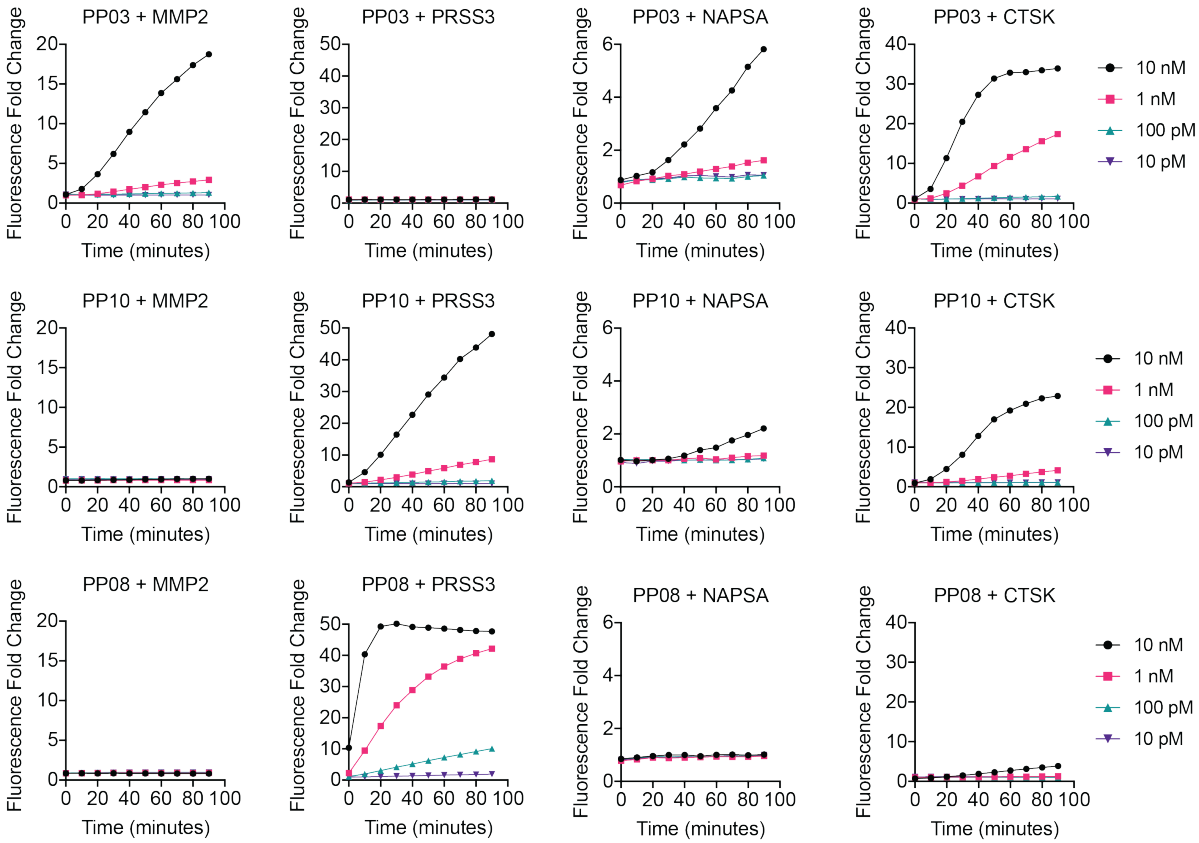

Figure S7: Protease nanosensors exhibit distinct specificities for proteases of different catalytic classes. Sample plots showing fluorescence increase over time after incubation of fluorogenic peptide substrates (PP03, top; PP10, middle; and PP08, bottom) with a metalloprotease (MMP2), serine protease (PRSS3), aspartic protease (NAPSA) and cysteine protease (CTSK) at enzyme concentrations ranging from 10 pM to 10 nM.

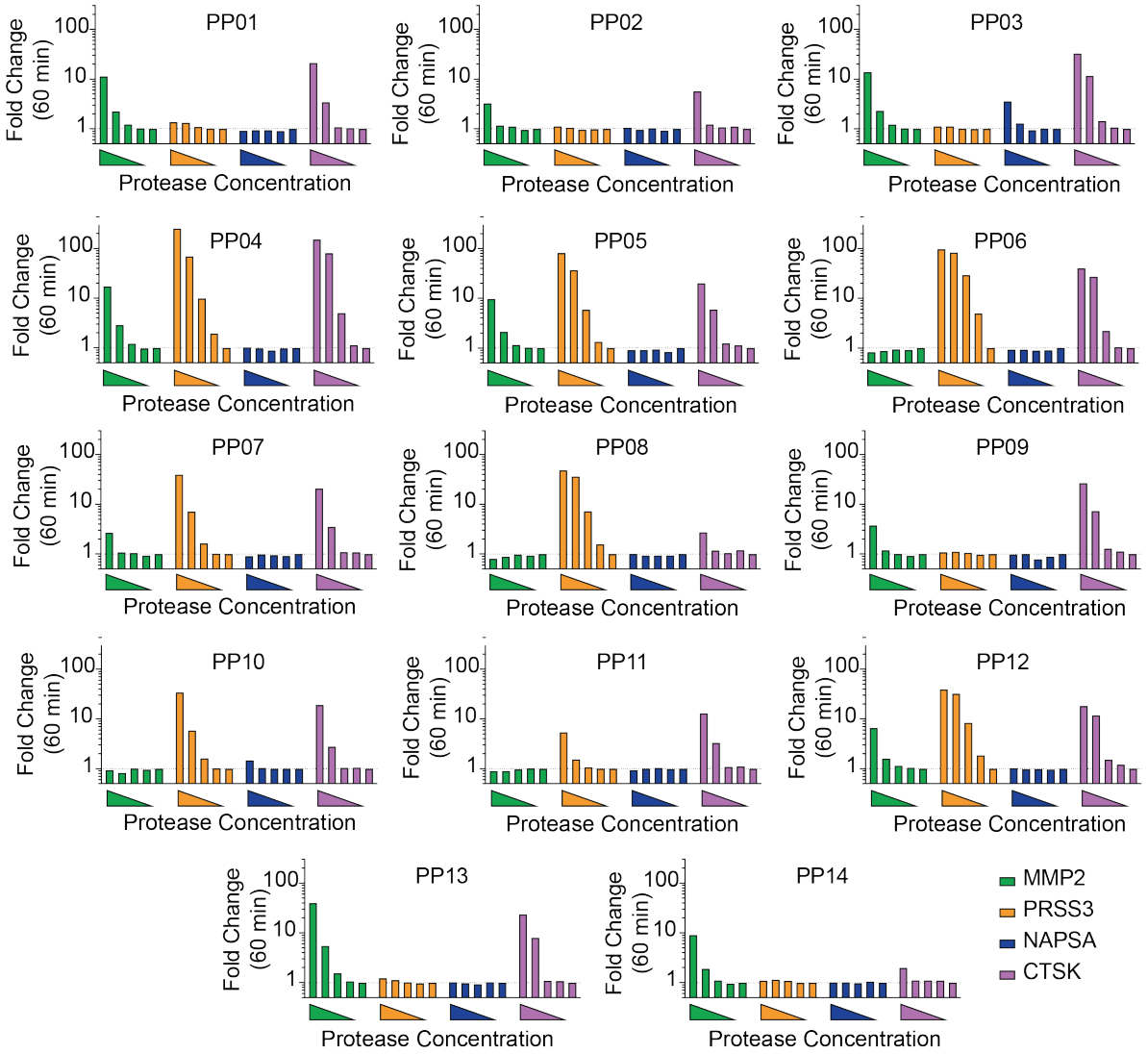

Figure S8: Protease nanosensors provide broad coverage of proteases across multiple catalytic classes. A metalloprotease (MMP2, green), serine protease (PRSS3, orange), aspartic protease (NAPSA, blue) and cysteine protease (CTSK, purple) were incubated at 10 nM, 1 nM, 100 pM, 10 pM, or 0 pM with quenched fluorescent versions of each nanosensor (PP01-14), such that fluorescence was activated in response to proteolytic cleavage. Fold change of fluorescence relative to peptide incubated without protease at 60 minutes is shown. Dotted line at fold change = 1.

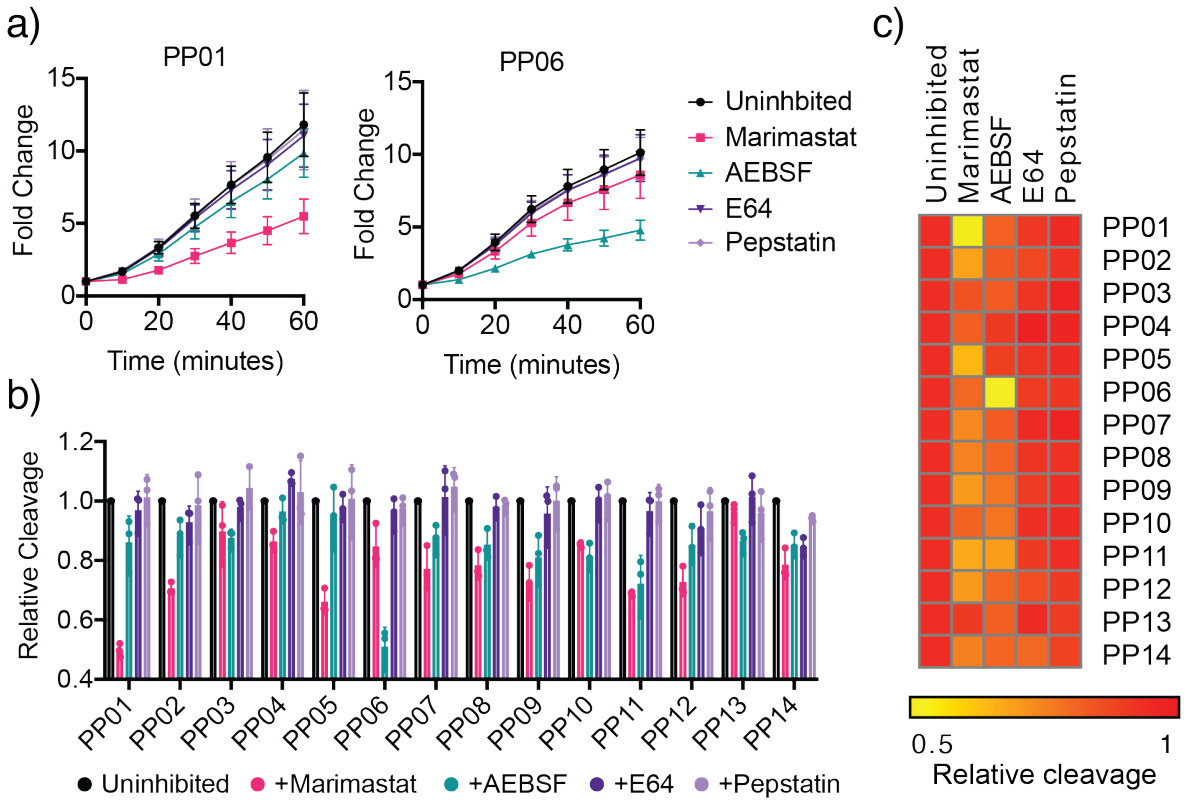

Figure S9: Metalloproteases and serine proteases are active in *Tsc2*-deficient 105K cell lesions at neutral pH. a) Fluorescence increase over time of a sample metalloprotease-sensitive (PP01, left) and serine protease-sensitive (PP06, right) peptide incubated with homogenates of 105K cell tumors at neutral pH with or without inhibitors against metalloproteases (marimastat), serine proteases (AEBSF), cysteine proteases (E64), or aspartic proteases (pepstatin). b-c) Substrate cleavage after 30 minutes in homogenates diluted in neutral pH buffer incubated with different protease inhibitor classes, relative to uninhibited homogenates.

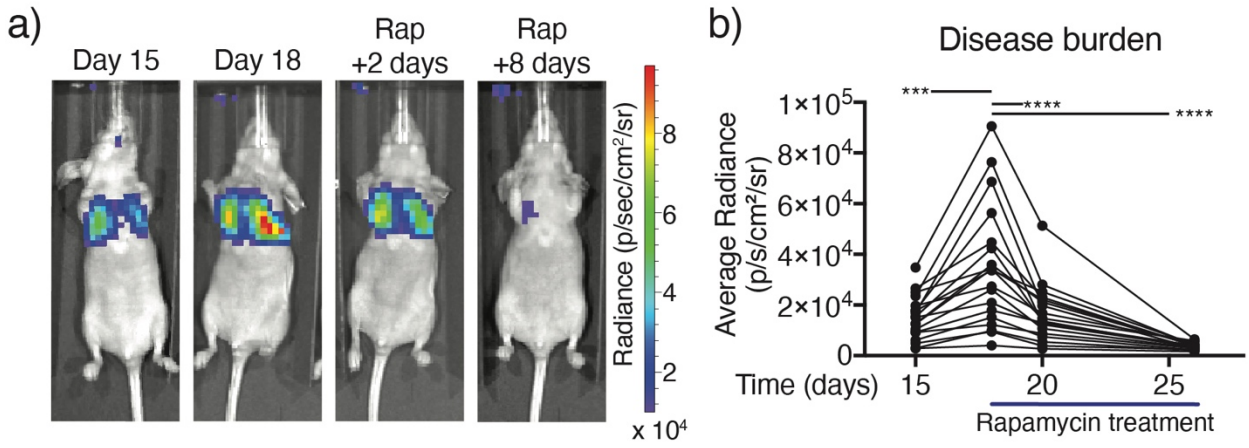

Figure S10: Rapamycin induces disease regression within two days after initiation. A) Representative IVIS images of a LAM mouse treated with rapamycin (3 mg/kg) after 18 days of disease development. B) Quantification of disease burden, as assess by IVIS imaging. ****$P <$ 0.0001 by paired two-tailed *t* test.

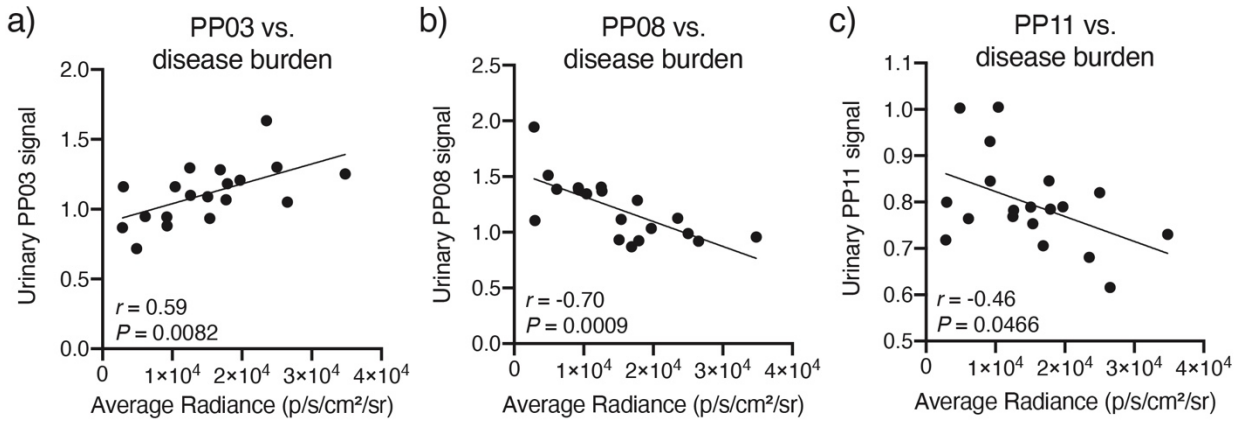

Figure S11: Multiple activity-based nanosensors correlate with disease burden. Correlation (Pearson r) of mean scaled urinary peak area ratio of PP03 (a), PP08 (b) and PP11 (c) with disease burden, as assessed by IVIS bioluminescence imaging, 14 to 15 days after 105K-Luc cell injection.

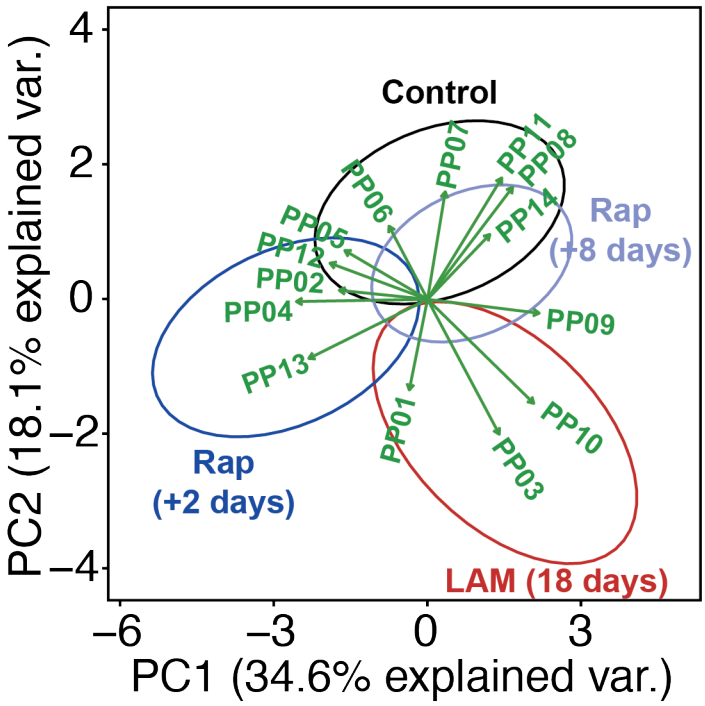

Figure S12: Disease progression and rapamycin treatment result in distinct nanosensor cleavage profiles. PCA loadings (green arrows) showing the contribution of each nanosensor to each principal component in figure 4c.

Nanosensor	Substrate sequence	Metallo-protease sensitivity (nM)	Serine protease sensitivity (nM)	Aspartic protease sensitivity (nM)	Cysteine protease sensitivity (nM)
PP01	GGPQGIWGQC	0.1	1	ND	1
PP02	GGPVGLIGC	10	ND	ND	1
PP03	GGPVPLSLVMC	0.1	ND	1	0.1
PP04	GGPLGLRSWC	0.1	0.01	ND	0.1
PP05	GGPLGVRGKC	1	0.01	ND	0.1
PP06	GGfPRSGGGC	ND	0.01	ND	0.1
PP07	GGLGPKGQTGC	10	0.1	ND	1
PP08	GGGSGRSANAKGC	ND	0.01	ND	10
PP09	GGKPISLISSGC	10	ND	ND	0.1
PP10	GGILSRIVGGGC	ND	0.1	10	1
PP11	GGSGSKIIGGGC	ND	1	ND	1
PP12	GGPLGMRGGC	1	0.01	ND	0.01
PP13	GGP-(Cha)-G-Cys(Me)-HAGC	0.01	10	ND	1
PP14	GGAPFEMSAGC	1	ND	ND	10

Table S1. Substrate sequences and protease class sensitivity. Cha, 3-Cyclohexylalanine; Cys(Me), methyl-cysteine; lowercase letters, D-amino acids; ND, no cleavage detected; Sensitivity is defined as minimum enzyme concentration required to yield a fluorescence fold change greater than 1.2 after 60 minutes.